Polymer 51 (2010) 1437–1449

Contents lists available at ScienceDirect

Polymer

journal homepage: www.elsevier.com/locate/polymer

The quantitative analysis of nano-clay dispersion in polymer nanocomposites by small angle X-ray scattering combined with electron microscopy

Jayita Bandyopadhyay, Suprakas Sinha Ray*

DST/CSIR Nanotechnology Innovation Centre, National Centre for Nano-Structured Materials, Council for Scientific and Industrial Research, Pretoria 0001, South Africa

ARTICLE INFO

Article history:
Received 18 November 2009
Received in revised form
6 January 2010
Accepted 12 January 2010
Available online 20 January 2010

Keywords:
Nanocomposites
Dispersed structure
Small angle X-ray scattering and scanning transmission electron microscopy

ABSTRACT

The main objective of this work is to propose a new approach for the quantitative analysis of the degree of dispersion of clay particles in the polymer matrix by small angle X-ray scattering (SAXS) combined with electron microscopy. Due to the low temperature processibility and good thermal stability, poly[(butylene succinate)-*co*-adipate] (PBSA) was chosen as a model polymer matrix for this study. The nanocomposites of PBSA with four different weight percentages of organically modified montmorillonite (OMMT) loadings were prepared via melt-blending method. The dispersed structure of the clay particles in the PBSA matrix was studied by SAXS. Results show that the clay particles are nicely dispersed in the case of all nanocomposites. However, with a systematic increase in clay loading, the dispersed clay structure of the nanocomposites changes from a highly delaminated to a flocculated and then to a stacked intercalated one. The probability of finding neighboring clay particles in the PBSA matrix as well as their thickness was calculated using the Generalized Indirect Fourier Transformation technique developed by Glatter and the modified Caillé theory proposed by Zhang. The morphology of the nanocomposites was also extensively studied by scanning transmission electron microscopy (STEM). In the case of all nanocomposites, SAXS results were in good agreement with STEM observations. Finally, a correlation between the predicted morphology of nanocomposites and their melt-state rheological properties is reported.

© 2010 Elsevier Ltd. All rights reserved.

1. Introduction

Over the last few years, much effort has been made to develop high-performance novel polymeric materials through the benefit of nanotechnology. One such niche area is polymer nanocomposite technology or more particularly clay-containing polymer nanocomposites (PNC) because of the low volume (≈5%) additions of layered silicate particles into the polymer matrix, which results in substantial property enhancements with respect to the neat polymer matrix [1]. During recent years, nearly all types of polymer matrices have been used for the preparation of nanocomposites with both pristine and organically modified clays [2–6]. Research results have shown some interesting and improved properties over those of the neat polymer matrices [2–6]. However, in most cases, the resulting composite mechanical properties fail to meet expectations as predicted theoretically. The main reason for this is that the layered silicate particles are dispersed in the polymer matrix as aggregates. If the silicate particles are not dispersed at nano-level, the active surface area will not increase sufficiently for polymer-filler interaction and as a result very small amount of stress will be transferred between the filler and the matrix. Therefore, prior to the establishment of the structure–property relationship in the case of clay-containing polymer nanocomposites, a detailed understanding of silicate layer-dispersion into the polymer matrix is of prime importance.

Recently, various techniques, such as wide-angle X-ray diffraction [7], Fourier transform infrared spectroscopy (FTIR) [8], nuclear magnetic resonance (NMR) [9], optical microscopy [10], dielectric spectroscopy [11], scanning and transmission electron microscopy [12], melt-state rheology [13], etc., have been used to study the degree of dispersion of silicate layers in various polymer matrices. However, there are only a few reports where X-ray scattering techniques have been used to study the degree of dispersion of silicate layers in the polymer matrix in detail. Over the last decade, the small angle X-ray scattering (SAXS) has been extensively used to study the phase dispersion in matrices, polymerization, emulsification, colloidal stabilization, shear-induced structures, polymer crystallization, and the phase domain behavior in polymers [14]. In the case of nanostructured materials such as clay-containing polymer nanocomposites, one of the biggest advantages of SAXS is that it probes materials with subnanometer resolutions (1–100 nm)

* Corresponding author. Fax: +27 12 841 2229.
E-mail address: rsuprakas@csir.co.za (S. Sinha Ray).

0032-3861/$ – see front matter © 2010 Elsevier Ltd. All rights reserved.
doi:10.1016/j.polymer.2010.01.029

and at the same time uses a large sample size, i.e., which covers a large number of nanoparticles [15].

For example, Schaefer and Beaucage used SAXS technique to determine the porous surface area of the resorcinol-formaldehyde aerogels and correlate SAXS data interpretation with the BET results [16]. Hua and Beaucage investigated the micro- and meso-pore size range of silica aerogels by SAXS [17]. In the case of clay-containing polymer nanocomposites, SAXS has been used to determine the structure of the nanocomposites, either from the peak shift toward a lower scattering angle side or from the power law dependence [18]. Koerner and co-authors studied the uniaxial elongation behavior of polymer nanocomposites in combination with the in-situ X-ray scattering [19]. Lincon et al. used SAXS technique to study the temperature dependence of polymer crystalline morphology and the effect of curing on the intercalated structure of the nanocomposites [20,21]. Chin et al. studied the effect of curing temperature and concentration of curing agent on the epoxy-clay nanocomposites by means of shifting scattering peak [22]. From the broadening of SAXS peaks, Nawani et al. concluded that the average stack size of clay particles was decreased due to the partial delamination of silicate layers in the EVA matrix. They also investigated the effect of mixing time on the clay dispersion using SAXS [23]. Inspite of these reports, SAXS analysis with the variation of temperature showed that for ethylene–propylene copolymers (EP) during cooling from melt the lamellar structure became more well-defined. In the case of the EP-POSS (polyhedral oligomeric silsesquioxane) nanocomposites, the higher POSS content hindered the formation of that EP-crystalline lamellae [24]. The orientation behavior of Nylon 6/MMT nanocomposite in the molten state during steady shear, afterward relaxation and during non-isothermal crystallization was also studied by SAXS [25].

On the basis of this information, Causin et al. [26] first used the extended Hosemann's model [27] to analyze experimentally obtained SAXS patterns for the quantification of silicate layer-dispersion in polypropylene (PP) and poly(butene) (PB) matrices. According to them, the nanocomposite consists of alternating high electron density silicate layers with low electron density regions interposed by considering the geometrical similarity in morphological distribution to that of lamellae. The influence of additives and processing conditions on the extent of nano-clay dispersion was explained with quantitative data such as the number of clay layers, and the interlayer spacing and its distributions. Model parameters were verified with extensive transmission electron microscopy (TEM) and wide-angle X-ray studies. Preschilla et al. [28] also used Hosemann's model for the evaluation of nano-clay dispersion depending on various processing routes in different PP homopolymer, random copolymer, and high impact PP–ethylene propylene rubber (EPR). Yoonessi et al. [29] studied the dispersed microstructure of the layered silicate particles in the nanocomposites by small angle neutron scattering (SANS), ultra-small angle neutron scattering (USANS), SAXS, and high-resolution transmission electron microscopy (HR-TEM). They calculated the mean number of individual clay platelets per tactoid both by fitting SANS data to the stacked-disk model and by measuring directly from HR-TEM images. According to them, the number of tactoids as well as individual clay platelets present in the nanocomposites decreased slightly as the clay loading increased from 0.5 to 2 wt%. Further, the mean number of platelets per tactoids increased with clay loading. However, they did not report how these structures were related to the final properties of the nanocomposites. Very recently, Drummy et al. [30] have used a combined SAXS and electron tomography approach to study the dispersion of layered silicate particles in an epoxy matrix.

The poly[(butylene succinate)-*co*-adipate] (PBSA) is a synthetic aliphatic polyester and is synthesized by the polycondensation of butane-1,4-diol in the presence of succinic and adipic acids with relatively low production cost and satisfactory mechanical properties equivalent to that of polyolefins [31]. The PBSA, compared with poly(butylene succinate) (PBS), is more susceptible to biodegradation because of its lower crystallinity and more flexible polymer chains [32]. It also has excellent processibility, so that it can be processed in the field of textiles into melt blow, multifilament, monofilament, flat, and split yarn, and also in the field of plastics into injection-moulded products. It is, thus, a promising polymer for various applications.

This paper will discuss a new approach to estimate quantitatively the degree of dispersion of silicate layers in the polymer matrix using SAXS and correlate the predicted morphology with the melt-state rheological properties of nanocomposites. The nanocomposites of PBSA with four different OMMT loadings were prepared by a melt-blending technique. The nature of layered silicate dispersion in the nanocomposites was characterized using a combined SAXS and scanning transmission electron microscopy (STEM). Further, the structure of dispersed clay particles and the electron density distribution along the thickness cross-section of clay lamellae were studied by Generalized Indirect Fourier Transformation (GIFT) along with modified Caillé theory and the deconvolution technique proposed by Glatter. Finally, the predicted morphology of the nanocomposites was correlated with their melt-state rheological properties.

2. Experimental part

2.1. Materials

The PBSA used in this study is a commercial product from Showa High Polymer (Japan), with the designation BIONOLLE #3001, which according to the supplier has a weight average molecular weight, $M_w = 190$ kg/mol, density = 1.23 g/cm^3 (ASTMD729), melt-flow index (MFI) = 1.8 gm/10 min (190 °C, ASTM1238), glass transition temperature, $T_g = -43.8$ °C, and melting temperatures, T_m's = 83.1 °C (first) & 94.5 °C (second). The molar ratio of succinate unit to the adipate unit is ~ 4:1 and the content of the coupling agent (hexamethylene diisocyanate) unit is ~0.5 mol%. Organoclay used in this study was Cloisite® 30B (C30B), purchased from the Southern Clay Products, USA. According to the supplier, the pristine MMT is modified with 30 wt% of methyl tallow bis(2-hydroxylethyl) quaternary ammonium salt. The reason for choosing C30B as an OMMT in this study is that it has the closest value of the polar solubility parameter of the surfactant (21.5 J$^{1/2}$ cm$^{-3/2}$) with that of PBSA (23.8 J$^{1/2}$ cm$^{-3/2}$) [33]. Prior to melt-blending, the polymer was dried under vacuum at 60 °C for 48 h and C30B at 75 °C for 4 h. The molecular structures of PBSA and the surfactant used to modify pristine clay are, respectively, presented in parts (a) and (b) of Fig. 1.

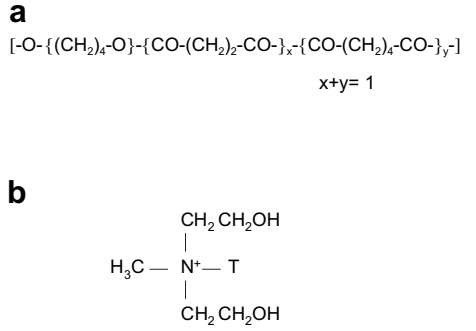

Fig. 1. (a) The molecular structure of poly[(butylene succinate)-*co*-adipate] and (b) chemical structure of bis(2-hydroxylethyl) quaternary ammonium used to modify pristine MMT. 'T' represents tallow (~65% C18; ~30% C16; ~5% C14).

The thermal stabilities of the PBSA and the C30B powder were investigated by a thermogravimetric analyzer (TGA, TA Instrument Q500 model), under air atmosphere. The samples were heated to 125 °C at a ramp rate of 20 °C/min, kept at 125 °C for 15 min, and then heated to 700 °C at a ramp rate of 20 °C/min. From TGA scans, it is clear that there are only 0.4 and 1.1% (this is due to adsorbed water) weight losses for PBSA and C30B, respectively, at 125 °C after 18 min.

2.2. Nanocomposite preparation

PBSA nanocomposites (PBSANC) with four different weight percentages of C30B loading were prepared via a melt-mixing technique. PBSA was first melted in a Polylab Thermohaake-batch mixer (capacity = 50 g, counter rotating rollor rotor 600, 557–1030) at 125 °C (set temperature) for 1.5 min with a rotor speed of 60 rpm. The C30B powder was then added for 1 min and then blended for 6.5 min. The PBSA nanocomposites (PBSANCs) with four different C30B loadings of 3, 4, 5, and 6 wt% were abbreviated as PBSANC3, PBSANC4, PBSANC5, and PBSANC6, respectively. The dried nanocomposite strands were then converted into films with a thickness of 0.4–1.5 mm by pressing at 2 torr pressure at 125 °C for 2 min using the Craver Laboratory Press.

2.3. Small angle X-ray scattering (SAXS)

SAXS experiments were carried out by an Anton Paar SAXSess instrument, operated at 40 kV and 50 mA with the line collimation geometry. The radiation used was a Ni filtered CuK_{α} radiation of wavelength 0.154 nm (PAN Analytical X-ray source). Intensity profiles were obtained with a slit collimated SAXSess and recorded with a two-dimensional imaging plate. The sample-to-detector distance was 264.5 mm and covers the length of the scattering vector (q) from 0.084 to 28 nm^{-1}. The read-out angles are calculated from the pixel size, and the obtained q-scale was cross-checked by measuring silver behenate whose equidistant peak positions are known. SAXS data were collected at room temperature. All samples were exposed under X-ray for 5 min (we have chosen this time because after 5 min there was no significant effect of exposure time on peak intensity) in order to check the dispersion characteristic of the silicate particles in the PBSA matrix. Prior to SAXS analyses, both pure PBSA and nanocomposite samples were annealed at 50 °C under vacuum for 21 h. The thickness of the samples varied roughly between 0.3 and 0.4 mm. The exposure time of pure C30B powder was chosen to be 10 s in order to get rid of forward scattering.

2.4. Scanning transmission electron microscopy (STEM) study

The degree of dispersion of silicate layers in the PBSA matrix was evaluated by STEM. For the STEM studies, ~60–75 nm thick compression-moulded nanocomposite lamellae were prepared using a Focused Ion Beam FEI Helios Nanolab SEM (FIB-SEM, FEI Company) (Gallium ion source and beam current was 0.92 mA), operated at 30 kV. To avoid damage, the sample surface was first covered with a platinum deposition. Bright-field STEM images of various nanocomposite samples were taken in a FEI Helios Nanolab SEM using STEM-II detector.

2.5. Rheological study

The behavior of polymeric materials is based on the combination of both the viscous and the elastic portions, and therefore, they are known as viscoelastic material. The rheological experiments in molten–state reveal information about the flow behavior of such materials since any large deformation produced by shear forces cause polymeric materials to flow. For any oscillatory test it is necessary to determine the amplitude of oscillation for which any structural modification is reversible. On the other hand, the frequency sweep results are useful to investigate the time-dependent shear behavior since the frequency is the inverse value of the time. Short-term behavior is simulated by the rapid motion (i.e., at high frequencies) and the long-term behavior by slow motion (i.e., at low frequencies). It is obvious that any change in property is directly related to the structure of the nanocomposite. Therefore, it is very important to correlate the morphological changes of the nanocomposites containing different amount of clay with their rheological properties.

The melt-state flow behaviors of the pure PBSA and various nanocomposites were studied by using an Anton Paar rheometer model MCR-501 with parallel plate (PP-25) geometry. To do the dynamic oscillatory measurements one should first determine the amplitude of oscillation in the linear viscoelastic (LVE) region, where any structural change is supposed to be reversible. Hence, the strain amplitude sweep experiments of all samples were performed at 125 °C with a constant angular frequency (ω) = 6.28 rad/s in the varying strain window 0.01–100%. The frequency sweep experiments were carried out at the same temperature with a strain amplitude (chosen from the LVE region) of 0.1% in the frequency rage 100–0.01 rad/s. The thixotropic oscillatory experiments were also performed at 125 °C with the three intervals. The first interval was the pre-shear interval where samples experienced constant strain and frequency of 0.1% and 6.28 rad/s, respectively for 120s. In the second interval, in order to break the structure, constant strain of 50% was applied for 60 s, at a constant $\omega = 6.28$ rad/s. In the regeneration interval, i.e., in the third zone, the same strain and frequency as the first interval were applied for 1000 s.

3. Theoretical background

3.1. Form and structure factors

The SAXS is a powerful tool used to determine the size, shape, and internal structure of the particle system of sizes ranging from 1 to 100 nm. The SAXS analysis is mainly applicable for randomly oriented and statistically distributed particle systems. Hence, their three-dimensional scattering pattern represents the orientational average of their structure. Only in the case of three types of ideal symmetry; i.e., for spherical, cylindrical, and lamellar structures with a centrosymmetric scattering length density distribution, there is no loss of information due to the orientational averaging [34]. Now this orientational averaging is radially symmetric and can therefore be reduced to the one-dimensional angle-dependent scattering intensity function $I(q)$ presented by equation (1).

$$I(q) = 4\pi \int_0^{\alpha} p(r) \frac{\sin qr}{qr} \mathrm{d}r \tag{1}$$

where q is the scattering vector and can be related to the scattering angle (θ) and wavelength (λ) by equation (2).

$$q = \frac{4\pi}{\lambda} \sin\theta \tag{2}$$

The $p(r)$ in equation (1) represents a pair-distance distribution function of the electrons; or in other words, the radial or spherical symmetric correlation function of electron density differences weighted by $4\pi r^2$. It shows directly the probability of

finding a pair of electron densities at a particular distance *r*. All the information available from the experimental curves in the small angle region is in reciprocal space since $q\alpha 1/\lambda$. Therefore, it is difficult to get direct information about the form and structure factors of the particles.

The form and structure factors can be explained as follows: Let us consider a composite particle consist of sub-particles with a fixed orientation. The positioning of the centres of mass of the sub-particles may be designated by $r_1, r_2 \ldots r_j \ldots\ldots r_N$. The scattered wave's amplitudes from these sub-particles can be designated by (with respect to each centre) $F_1, F_2 \ldots\ldots, F_j \ldots\ldots, F_N$. The positions of the sub-particles are each accounted for by an additional phase factor e^{-iqr_j}. Therefore, the total amplitude of the composite particle is

$$F(q) = \sum_{1}^{N} F_j(q)\cdot e^{-iqr_j} \tag{3}$$

In general, each amplitude will have a phase too,

$$F_j = |F_j|\cdot e^{i\varphi_j} \tag{4}$$

Then the intensity is

$$I(q) = FF^* = \left\langle \sum_{j=k}\sum F_jF_k^*\cdot e^{-iq(r_j-r_k)} \right\rangle + 2\left\langle \sum_{j\neq k}\sum |F_j||F_k|\cos\left(qr_{jk}+q_k-q_j\right) \right\rangle \tag{5}$$

The double sum contains *N* terms with $j = k$, the phase factor consequently vanishing. The remaining term with $j \neq k$ represent the interference between the sub-particles according to the relative distance $r_{jk} = (r_j - r_k)$. Since each pair is counted twice with $r_{jk} = -r_{kj}$, only the real part is accountable. Therefore, the intensity contribution with $j = k$ can be considered as form factor and that with $j \neq k$ can be considered as structure factor.

3.2. Generalised indirect Fourier transformation (GIFT)

The real space transformation of the SAXS data (after desmearing) by inverse Fourier transformation (IFT) of the Fredholm integral equation (see equation (1)) can determine the parameters such as $p(r)$; from where the form and structure factors can be evaluated. But doing IFT is impossible here because of the termination effect of *q*-scale and the influence of a remaining background scattering. These may cause some strong artificial oscillations ("Fourier ripples") in the $p(r)$ function and make the analysis useless [35,36]. At small *q*-values the measurement is limited by the unscattered primary beam and at large *q*-values by the progressive decrease of the signal-to-noise ratio. The scattered intensity is usually determined at discrete points. According to the counting statistics, the standard deviation of each data point is equal to the square root of the number of pulses registered by the counter. The termination effect can be reduced by the extrapolations of the scattering curve. For example, the Guinier approximation can be used to extrapolate the scattering curve toward a zero angle provided the first data point is measured at a very small angle. The extrapolation toward a large angle can sometimes be performed with Porod's law. But the termination effect can be minimized by the indirect Fourier transformation method developed by Glatter [37,38]. In most cases researchers are interested in studying the structure of particles dispersed in solution and to avoid background scattering the solvent is taken as a background, and then the $I(q)$ of the solvent is subtracted from the $I(q)$ of the solution. In the case of polymer nanocomposite, in order to get information about the dispersed nanoparticles, the pure polymer should be taken as a background and subtracted from the scattering intensity of the nanocomposite. The indirect Fourier transformation takes into account the following factors: single-step procedure, optimized general function system, weighted least square approximation, error propagation, minimization of the termination effect, and consideration of the physical smoothing condition given by the maximum intra-particle distance [36]. Therefore, for smoothing conditions it is necessary to estimate the upper limit of the largest particle dimension, i.e. D_{max}. Therefore, if

$$r \geq D_{max}, p(r) = 0 \tag{6}$$

Now, a function system should be defined in the range $0 \leq r \leq D_{max}$ and a linear combination of these functions should provide the $p(r)$. Therefore,

$$p_A(r) = \sum_{\upsilon=1}^{N} c_\upsilon\varphi_\upsilon(r) \tag{7}$$

where the suffix "*A*" denotes only that this $p(r)$ is approximated. *N* is the number of functions and should be chosen sufficiently in order to cover the range $0 \leq r \leq D_{max}$; c_υ be the unknowns and can be determined by a weighted least square approximation of the experimental data. $\varphi_\upsilon(r)$ are chosen as cubic *B*-spline functions, and they can be defined as multiple convolution products of a step function, representing curves with a minimum second derivative. Each individual spline function can be subjected to Fourier transformation (T_1), wavelength integral (T_2), slit-length integral (T_3), and slit-width integral (T_4). The intermediate result after Fourier transformation of all the splines represents the scattering intensity without the collimation effect corresponding to a distance distribution $\varphi_\upsilon(r)$. Therefore, the intensity without the collimation effect $[\Psi_\upsilon(q)]$ can be expressed as

$$\Psi_\upsilon(q) = T_1\varphi_\upsilon(r) \tag{8}$$

The smeared intensity (i.e., after adding the collimation effect) can be obtained after execution of T_2, T_3, and T_4 as

$$\chi_\upsilon(q) = T_4T_3T_2\Psi_\upsilon(q) = T_4T_3T_2T_1\varphi_\upsilon(r) \tag{9}$$

So $\chi(q)$ represents the approximated scattering data from a particle with maximum distance, D_{max}. The next step is the stabilization of these coefficients. The stabilized least squares condition is given below

$$L + \lambda_L N_{c'} = \text{minimum} \tag{10}$$

with

$$L = \int_{q_1}^{q_2} \frac{\left[I_{exp}(q) - \sum_{\upsilon=1}^{N} c_\upsilon\chi_\upsilon(q)\right]^2}{\sigma^2(q)}\,dq \tag{11}$$

and

$$N_{c'} = \sum_{\upsilon=1}^{N-1}(c_{\upsilon+1} - c_\upsilon)^2 \tag{12}$$

Here, q_1 and q_2 are the first and last data points, $I_{exp}(q)$ is the experimental intensity, σ^2 is the estimated variance of the observed intensity, and λ_L is known as the stabilization parameter or

Lagrange multiplier [36–38]. The optimum fit to the observed data points is given by

$$I_A(q) = \sum_{\upsilon=1}^{N} c_\upsilon \chi_\upsilon(q) \tag{13}$$

$I_A(q)$ represents the approximated scattering curve, which should be similar to the experimental curve, $I_{exp}(q)$. Therefore, it can be concluded that the approximated distance distribution function $[p_A(r)]$ represents the $p(r)$ for the experimental curve.

In this study, we used the GIFT to evaluate the $p(r)$, which is consistent with the experimental scattering curve. Fig. 2 is the representative diagram of GIFT method for spherical particles. Here we consider $p(r)$ consists of N number of cubic B-spline functions. $p(r)$ shows directly the probability of finding a pair of electron densities at a particular distance 'r'. Therefore, each spline function can be considered as a distance between a pair of stacked silicate layers.

The beauty of the GIFT method is that the form and structure factors can be determined simultaneously from the measured scattering data with the correction for the instrumental broadening effect [39–41]. Therefore, to evaluate the $p(r)$ from the scattering curve, one has to consider the value of N, D_{max}, and λ_L. If there is a difference between $I_A(q)$ and $I_{exp}(q)$, then it is necessary to consider the effect of the structure factor.

D_{max} need not to be a perfect estimation of D. For rough estimation, $D_{max} \leq (\pi/q_1)$, where q_1 is the lowest scattering angle. A theoretical limitation for the number of functions $N = N_{max}$ follows from the sampling theorem. The main idea of the indirect Fourier transformation technique is to start with a large number of coefficients to guarantee a sufficient representation of the distance distribution function. For rough estimation, $N_{max} \leq (q_2 \cdot D_{max}/\pi)$, where q_2 is the maximum scattering angle. The stabilization parameter restricts the oscillation of the spline functions, in other word, oscillation of $p(r)$. It should be chosen in such a way that the approximated scattering curve (determined on the basis of the $p(r)$) possesses similar nature as the experimental scattering curve. Then only one can conclude the $p(r)$ related to the approximated scattering curve is the same as for the experimental scattering curve.

3.3. Determination of structure factor by applying modified Caillé theory conjugated with GIFT

The structure factor is determined according to the GIFT by using the modified Caillé theory for the lamellar phase. There are two theories that are applicable for the lamellar systems. The paracrystalline theory, a general theory for disorder of the first and second kind was developed by Hosemann & Bagchi [27] and Guinier [42]. This was the first attempt to deal with the disorder in multilamellar arrays. The paracrystalline theory of the first kind assumes that there are stochastic distance fluctuations around the well-defined mean layer positions of equal separation; i.e., the long-range order is maintained. The paracrystalline theory of the second kind describes the fluctuations of bilayer separations relative to the nearest neighbors of ideally flat bilayers. These fluctuations are not correlated and the long-range periodic order collapses [42]. On the other hand, the Caillé theory developed on the basis of thermodynamic theory of DeGennes for the smectic liquid crystal is preferable because it takes into account the bending of the bilayers in addition to fluctuations in the mean spacings between the bilayers [43]. The modified Caillé theory proposed by Zhang et al. takes into account the finite size of the lamellar stack [44]. This modification does not affect the quantitative results obtained by the original Caillé theory, but the modification is necessary to obtain better quantitative fits to the data and particularly for extracting the correct form factor, which could be used later to obtain an electron density profile.

As long as the bilayer is unilamellar, there exists a direct relationship between the electron density profile in the perpendicular direction to the midplane of the bilayer and the form factor. The lateral arrangement of multilamellar bilayers is represented by the structure factor and can be determined by either the paracrystalline or Caillé theory with a few parameters. It is necessary to assume either a form factor or a structure factor for the evaluation of the scattering data according to the paracrystalline or modified Caillé theory.

Frühwirth et al. implemented the modified Caillé theory on the GIFT in order to analyze the stacked lamellar systems [45]. This model is defined by three parameters: the number of coherently scattering bilayers (n), the repeat distance (d) of bilayers, and the

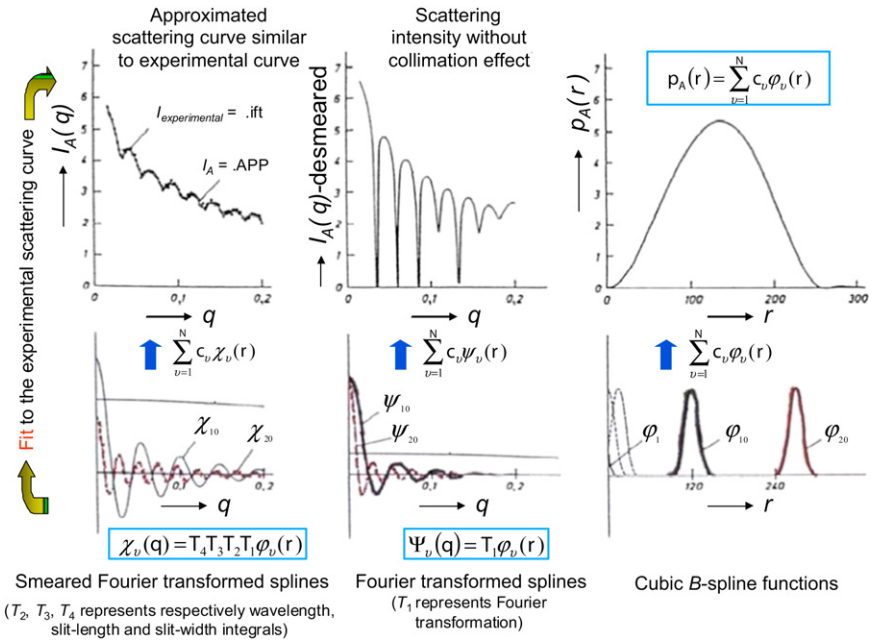

Fig. 2. The representative diagram of generalized indirect Fourier transformation (GIFT) method for spherical particle. Partly reproduced from ref. [36] with permission.

Caillé parameter (η_1). According to the modified Caillé theory, the structure factor can be expressed as

$$S(q) = n + \left\{ 2\sum_{m=1}^{n-1}(n-m)\cos(mqd)\exp \times \left[-\left(\frac{d}{2\pi}\right)^2 q^2\gamma\gamma \right](\pi m)^{-(d/2\pi)^2 q^2 \eta_1} \right\} \quad (14)$$

where γ is the Euler's constant (=0.5772). Again, the Caillé parameter η_1 can be expressed as

$$\eta_1 = \frac{q_1^2 k_B T}{8\pi (K_c B)^{1/2}} \quad (15)$$

where,

$$q = (2\pi/d) \quad (16)$$

K_c is the bending modulus and B is the bulk modulus for compression. Since the two moduli can't be determined independently from the scattering data, one can consider η_1 as a measure of flexibility of the bilayers. According to the author, increasing the number of bilayers causes higher and narrower peaks, and increasing the Caillé parameter leads to a faster decay of the peaks of higher order.

3.4. Determination of electron density distribution profile

The electron density for the lamellae can be written as (provided one assumes the lamellae are homogeneous along the basal plane)

$$\rho(r) = \rho_0 \cdot \rho_t(x) \quad (17)$$

Here, ρ_0 is a constant and x is the normal distance from the central plane in the lamellae. Therefore, $\rho_t(x)$ represents the electron density along the thickness cross-section profile [36]. There are two different ways to determine the electron density profile. In the conventional method, one has to determine the scattering amplitude from the scattering intensity by a simple square root operation. However, the main problem is the determination of the right sign—the so-called phase problem. The second method is the estimation of the electron density from the distance distribution function by a convolution square root technique. This method doesn't suffer the phase problem. Hosemann & Bagchi and Engel showed that for the lamellar system, the convolution square root has a unique solution (except for a factor ± 1) if the function has a finite range of definition and the function is symmetrical [36]. Glatter used the convolution square root method in a different way. He deconvoluted the approximated electron density distribution in order to get the distance distribution function for the highly symmetric systems (sphere, cylinder, or lamella). According to him, the electron density is approximated in its range of definition by a linear combination of a finite number of functions that have to be linearly independent in this range and can be expressed as

$$\overline{\rho}(r) = \sum_{i=1}^{N} c_i \varphi_i(r) \quad (18)$$

where N is the number of functions, r is the normal distance from the center of symmetry, $\varphi_i(r)$ is the equidistant step function (cubic B-spline of zero order) with a width ΔR allowing the analytical integration of the overlap integrals, and c_i is the height of the step functions. Equation (18) corresponds to a nonlinear distance distribution function (presented in equation (19)), which can be solved by an interactive stabilized way to describe the $p(r)$ function obtained from indirect Fourier transformation/GIFT [46].

$$\overline{p}(r) = \sum_{i=1}^{N} V_{ii}(r)c_i^2 + \sum_{i>k} V_{ik}(r)c_i c_k \quad (19)$$

Now if there is some deviation from the high symmetry, which is known as the polydispersity of the sample, then the $p(r)$ determined by the deconvolution (DECON) method (done by DECON software) will be slightly different than the $p(r)$ determined from GIFT. By estimating the amount of polydispersity one can achieve the best matching in $p(r)$ determined by GIFT and DECON. Therefore, the electron density distribution derived from DECON should represent the experimental scattering curve.

4. Results and discussion

4.1. Structural characterization by SAXS

The SAXS is a useful tool to determine the dispersion level of clay layers in the nanocomposites. Fig. 3 represents the normalized intensity (I) versus scattering vector (q) plots of pure C30B powder (see inset), compression-moulded sheets of PBSA, and various nanocomposite samples. According to Fig. 3, C30B powder has a characteristic peak at $q = 3.4$ nm^{-1}, which corresponds to a d-spacing of 1.85 nm as determined by equation (16).

Fig. 3 shows that pure polymer poses some crystalline arrangement in the very small angle region ($q = 0.5$ nm^{-1}), and this arrangement remains almost unaltered in the case of nanocomposites. On the other hand, in the case of nanocomposite samples, the disappearance of the characteristic clay peak in the SAXS patterns indicates that the crystal structure of clay particles are completely destroyed or silicate layers are disorderly oriented in the polymer matrix. However, many factors other than layer disorder orientation such as the small sample size (particularly sample thickness) and/or small tactoids may contribute to the featureless diffraction pattern that generally observed in the SAXS patterns of the nanocomposites.

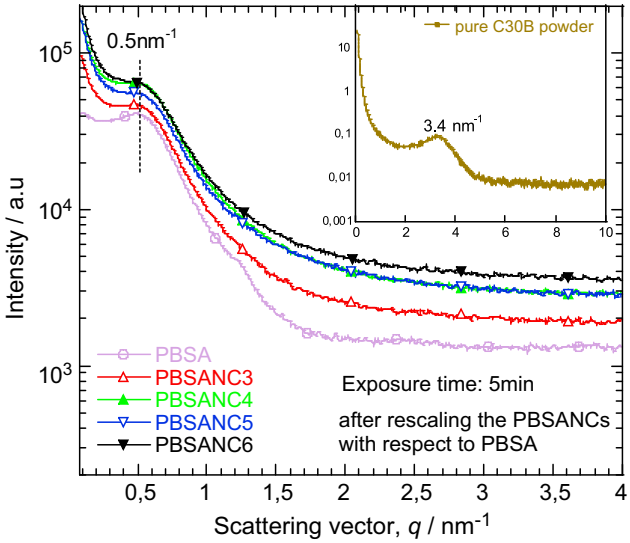

Fig. 3. Dark current subtracted small angle X-ray scattering (SAXS) patterns of pure C30B powder (in set) and compression-moulded (thickness ~ 0.3–0.4 mm) samples of pure polymer and various nanocomposites. The PBSA nanocomposites (PBSANCs) with four different C30B loadings of 3, 4, 5, and 6 wt%, were abbreviated as PBSANC3, PBSANC4, PBSANC5, and PBSANC6, respectively.

On the basis of the above results we can ask ourselves two very simple questions: First, is it possible to achieve a true exfoliated structure of the nanocomposites with a high clay content (e.g., with the clay loading of more than 3 wt%) although there are some favorable interfacial interactions between the polymer matrix and the surfactant used to modify the pristine clay surface? Second, how do the different degrees of delamination of silicate layers in the polymer matrix, with increasing the clay content, affect the nanocomposite properties? To find out those answers, detailed structural analyses and property measurements of various nanocomposite samples were carried out.

To have a more deeper understanding of the dispersion characteristic of clay particles in the PBSA matrix, extensive structural analyses for the model systems were conducted by SAXS. For the small angle analysis, first PBSA was taken as a background and then subtracted from the scaled intensity (without normalization) versus q curves for the nanocomposites. Finally, after Porod extrapolation, the constant background was subtracted, and the results are presented in Fig. 4. As described in Fig. 3, a small hump appears at $q = 0.5$ nm^{-1} (it also appears in Fig. 4) in SAXS patterns of all samples. This is due to the crystalline structure of the polymer. The reason for the appearance of such a hump after background subtraction is mainly due to the scale factor. According to Fig. 3, crystalline clay peaks are not visible for the PBSANCs. However, after background subtraction a less intense peak can be observed at $q = 1.36$ nm^{-1} in the SAXS patterns of all samples, as shown in Fig. 4. This is due to the scattering from the (001) plane of the dispersed clay particles in the PBSA matrix. In the case of PBSANCs, two different types of crystalline structures are supposed to be present in the small angle region. First, the lamellar structure of the polymer formed by the repetition of crystalline and amorphous portion, and second, the lamellar structure of the C30B made of crystalline silicate layers and organic modifiers [28]. Due to the intercalation of polymer chains in the clay galleries, the lamellar structure of C30B swells. According to the reciprocity theorem of scattering, those swallowed structures of lamellar C30B scatters in the small angle compared to the pure C30B, and, hence, the clay peak in the nanocomposite shifts toward the lower angle side. As already described in the theoretical section, the degree of dispersion of silicate layers in the polymer matrix can be considered as the thickness cross-section profile.

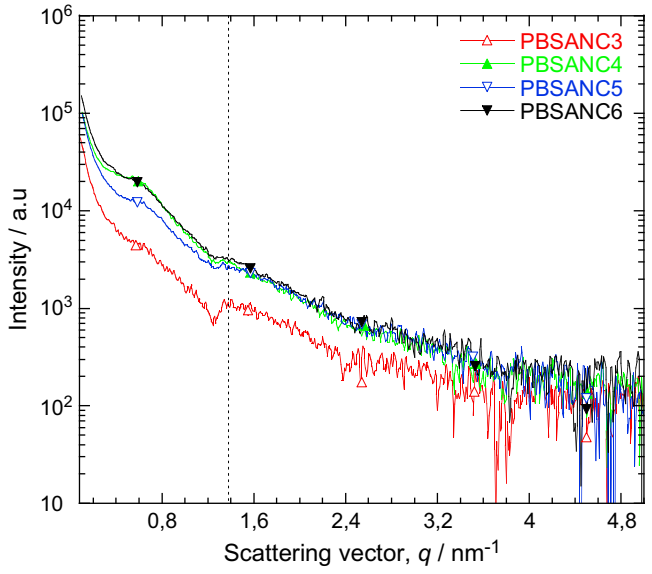

Fig. 4. Background and Porod subtracted scattering curves of model nanocomposite systems in the small angle region. The PBSA nanocomposites (PBSANCs) with four different C30B loadings of 3, 4, 5, and 6 wt%, were abbreviated as PBSANC3, PBSANC4, PBSANC5, and PBSANC6, respectively.

As described in the theoretical section, the sum of Fourier Transformed spline functions whose oscillations are restricted by Lagrange multipliers gives approximated desmeared scattering curves. After incorporation of the slit collimation effect it gives an approximated scattering curve that matches nicely with the experimental scattering curve and also provides $p(r)$. The modified Caillé theory in conjugation with GIFT provides information about the structure factor. As mentioned in the theoretical section, GIFT requires specification of N and D_{max}. The number of spline functions (N) used to cover the range of $p(r)$ was 40 and D_{max} for different nanocomposites are tabulated in Table 1. Initially, we determined $I_A(q)$ for 19 different λ_L – values and finally, we choose a particular λ_L – value for which $I_A(q)$ is almost similar to $I_{exp}(q)$. For better matching of $I_A(q)$ with $I_{exp}(q)$ it is now necessary to determine the effect of the structure factor for $q = 1.36$ nm^{-1}. The scattering curves represented in Fig. 5 with the extension ".ift" stand for experimental scattering curves after Porod subtraction, ".APP" stands for approximated scattering curves determined on the basis of GIFT conjugated with the modified Caillé theory, "PQE" stands for the form factor, and "SQE" stands for the structure factor. The ".ift" curves are the same with the scattering curves presented in Fig. 4. The structure factor was determined according to the modified Caillé theory for the lamellar phase for $q = 1.36$ nm^{-1}, number of silicate layers (n) = 5 to 20, spacing between layers (d) = 2 to 9, and Caillé parameter (η_1) = 0 to 1. Fig. 5 also shows that the approximated scattering curves coincide nicely with the experimental scattering curves. Therefore, the $p_A(r)$ from where $I_A(q)$ was estimated should be similar to the $p(r)$ representing $I_{exp}(q)$. The $p(r)$ of various PBSANCs is presented in Fig. 6. The regions with opposite signs of different electron density give negative contributions to $p(r)$, i.e., $p(r)$ can be negative in some regions as observed in the figure. The r-value at which $p(r)$ drops to zero indicates the largest single particle dimension [47]. According to the Fig. 6, the number of peaks increases with an increase in clay loading. The first exponentially decaying part where $p(r)$ first drops to zero represents the usual single particle form factor, and the other peaks can be explained as first, second, and third correlation maximums. These correlation maximums represent the average radial distance to the next neighboring domain, commonly known as long spacing. When the neighbors overlap, the peaks don't possess a tail; rather, a curve shows a maxima and minima. The results in Fig. 6 also show that in the case of PBSANC3 initially $p(r)$ decays to zero at $r = 3$ nm. But according to the inset of Fig. 6, the first correlation peak appears at 2.5, a second at 8 nm and a third one at ~10.5 nm, although first and third peaks are not so prominent. Therefore, PBSANC3 has three neighbors within a maximum distance of 11 nm (for better understanding see inset of Fig. 6).

With the increase in C30B loading, the neighboring particle domains start overlapping, and now it is difficult to determine the single particle's size. In the case of PBSANC4, the appearance of three correlation maxima indicate the presence of three neighbors, each possessing some portions that are overlapping each other within the maximum distance of 15 nm. On the other hand, in the case of PBSANC5, the probability of finding neighboring particles increases, and the neighbor could be present at distances $r = 1.7$, 3.6, 7.8, and 10.3 nm. The probability of finding neighboring particles in PBSANC6 are at distances $r = 3.6$, 7.9, 10.6, and 12 nm. However, according to Table 1, the maximum distance of finding neighbors (i.e. the maximum pair-distance, D_{max}) remains unaltered in PBSANC4, PBSANC5, and PBSANC6. From the above results it is now clear that the dispersion characteristics of C30B changes in PBSANCs with an increase in C30B loading. In the case of

Table 1
Results of SAXS analysis for various nanocomposite samples.

Sample[a]	Maximum pair-distance (D_{max})/nm	Mean number of layers (n)	Mean layer distance (d)/nm	Core diameter/nm[b]	Shell thickness/nm[c]
PBSANC3	11	5.6	4.5	$2 \times 3 = 6$	$2 \times 1.3 = 2.6$
PBSANC4	15	5.8	4.6	$2 \times 1.2 = 2.4$	$2 \times (3 + 1.8) = 9.6$
PBSANC5	15	5.7	4.4	$2 \times 1.3 = 2.6$	$2 \times (2.7 + 2.7) = 10.8$
PBSANC6	15	5.6	4.7	$2 \times 1.2 = 2.4$	$2 \times (3.6 + 1.2) = 9.6$

[a] Number on right side indicates the loading of C30B (wt%).
[b] Core diameter = twice the distance 'c' representing the core in Fig. 7.
[c] Shell diameter = twice the distance '(s1 + s2)' representing the shells in Fig. 7.

PBSANC3, the clay platelets are nicely delaminated since the probability of finding a neighbor is much less. However, the probability of finding neighboring particles at almost the same distances increases in the case of PBSANC4 as compared to PBSANC3. In the case of PBSANC5, the probability of finding neighbors increases both in the short and long distances. A tangent on the initial linear decaying portion can give a rough estimation of the largest single particle size (i.e., the smallest thickness of the dispersed clay layers) in PBSANC5 and it is ~1.5 nm. For PBSANC6, it is also ~1.5 nm. Therefore, PBSANC5 attains the maximum limit of delamination of clay layers and already the neighbors are overlapping like the flocculated nanocomposites' structure. After that, due to the geometric constraints, it is not possible to delaminate clay layers anymore and the clay stacking increases as in the case of PBSANC6. Again during determination of structure factor according to the modified Caillé theory for the lamellar phase for $q = 1.36\ nm^{-1}$, it was assumed that the number of silicate layers (n) present per stack is in between 5 and 20 and spacing between stacking (d) is within 2–9 nm. The GIFT analysis finally gives some estimation of n and d, and these parameters are reported in Table 1 as mean number of layers and mean layer distance, respectively. It can be observed that in the nanocomposites with different clay concentration the mean layer distance didn't change significantly. For this reason in Fig. 6 the position of the three main correlation peaks (~3.6, ~7.9 and ~10.6 nm) didn't change significantly. Another interesting

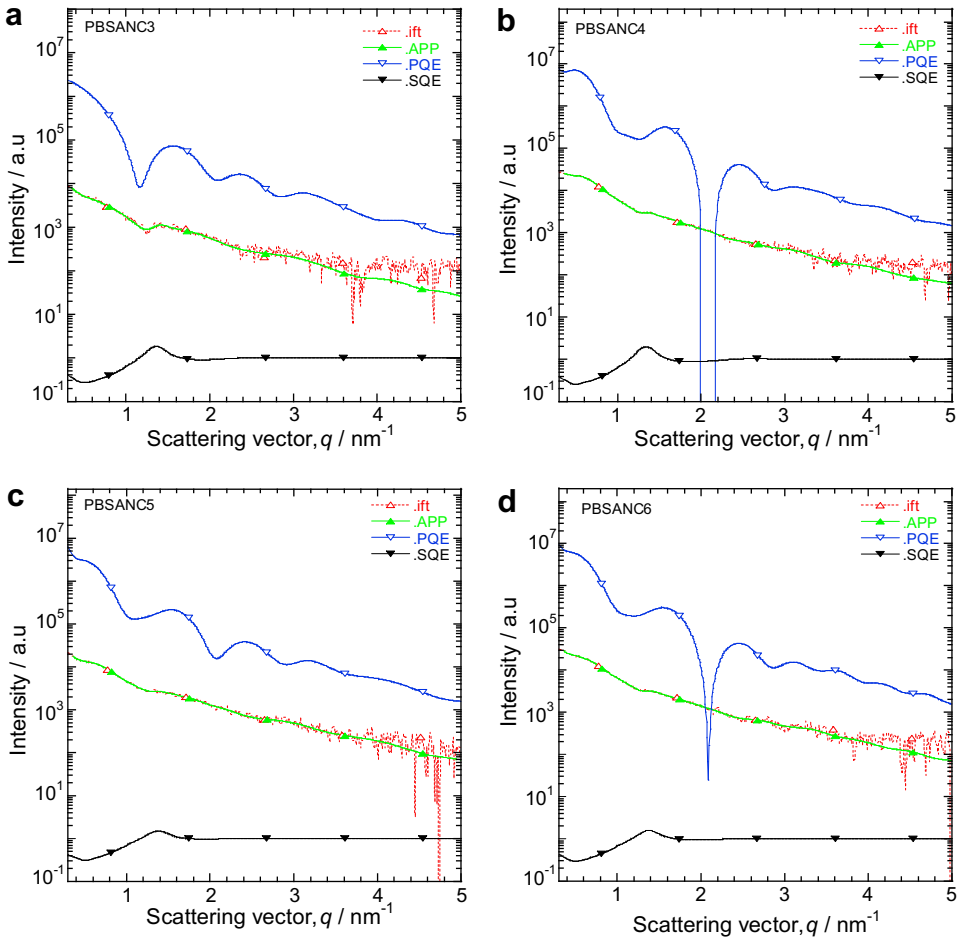

Fig. 5. ".ift" stands for experimental scattering curves after Porod subtraction, ".APP" stands for approximated scattering curves determined on the basis of GIFT conjugated with modified Caillè theory, "PQE" stands for form factor, and "SQE" stands for structure factor for: (a) PBSANC3 (containing 3 wt% C30B), (b) PBSANC4 (containing 4 wt% C30B), (c) PBSANC5 (containing 5 wt% C30B), and (d) PBSANC6 (containing 6 wt% C30B).

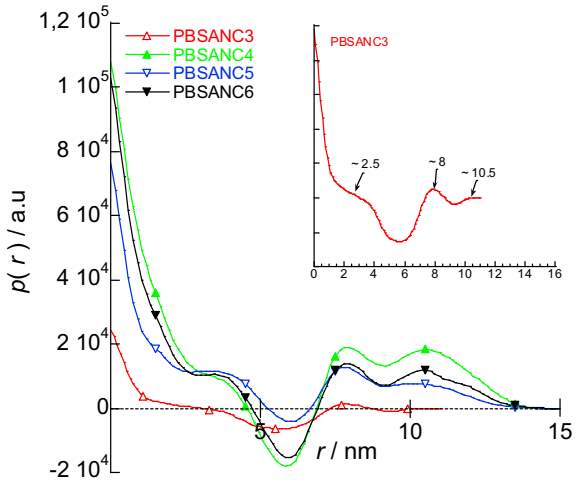

Fig. 6. The pair-distance distribution function, $p(r)$ for nanocomposites showing the probability of finding neighboring particles in systems with increase in C30B concentration. The PBSA nanocomposites (PBSANCs) with four different C30B loadings of 3, 4, 5, and 6 wt%, were abbreviated as PBSANC3, PBSANC4, PBSANC5, and PBSANC6, respectively.

observation is that the gap between the first and second correlation peak (i.e., d) is ~4 and that is between the second and third is ~3. This is in good agreement with the d-value presented Table 1.

The deconvolution of the $p(r)$ function provides an electron density profile of the thickness cross-section as presented in Fig. 7. According to Fig. 7 and Table 1, PBSANCs have a core-shell particle structure. When the clay platelets start peeling apart from each other in nanocomposites, these core-shell structures start to grow with the already peeled clay layers as a shell. PBSANC3 has a core thickness of approximately 6 nm and a shell layer thickness of 2.6 nm. In the case of PBSANC4, the core thickness decreases and the total shell thickness for the two shells increases dramatically. After that, there is no remarkable change in core thickness and also the total shell thickness for the two shells in both the PBSANC5 and PBSANC6. But PBSANC4 has a high electron density in the outer most shell, and PBSANC5 has two shells with almost the same electron density (see Fig. 7). In the case of PBSANC6, however, the outermost shell is becoming thinner since the contribution of neighboring particles increases, and the peeling effect attains its maximum limit. The mean number of layers and the mean distance between layers, estimated from the GIFT analysis, are also summarized in Table 1. For all nanocomposites, these two parameters remain almost the same. Therefore, the percolation threshold value of C30B loading in the case of C30B-containing PBSANCs is 5 wt%; for which the structure and, hence, it is expected the properties, of the nanocomposites change suddenly. So the structure of nanocomposites is changing especially from PBSANC4 to PBSANC5 and then from PBSACN5 to PBSANC6.

4.2. Scanning transmission electron microscopy observations (STEM)

To support the SAXS results, the samples were investigated by STEM because microscopy allows a qualitative understanding of the internal structure through direct visualization. For STEM analysis, for each nanocomposite on an average 15 samples were prepared and close to 55 images were taken (both in bright and dark fields). Fig. 8 shows the most representative bright-field STEM images of various PBSANCs in which black entities represent the dispersed silicate layers. The STEM image of PBSANC3 (Fig. 8(a)) shows that as a whole the clay particles are dispersed nicely in the PBSA matrix

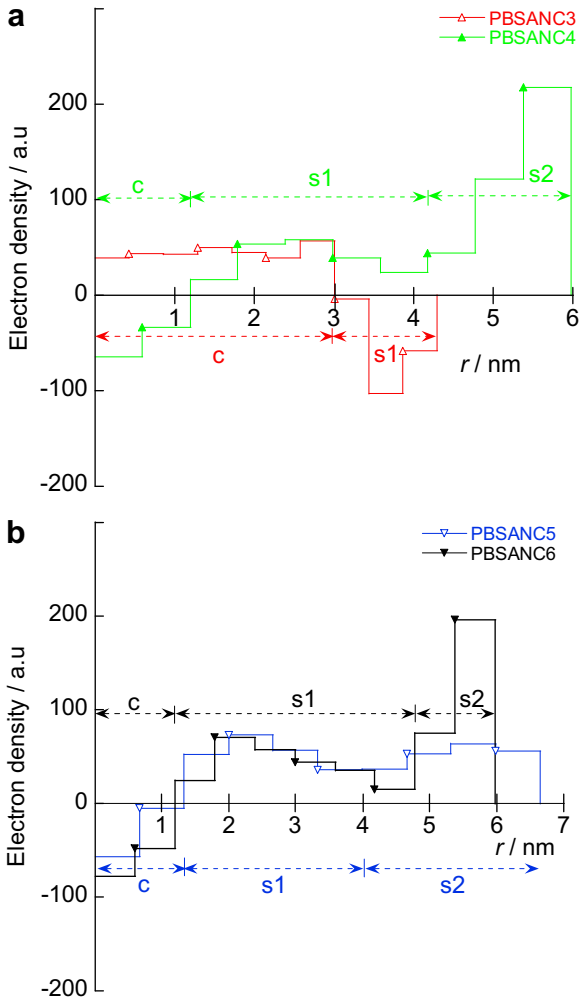

Fig. 7. Electron density profile of the model nanocomposites: (a) for PBSANC3 and PBSANC4 and (b) for PBSANC5 and PBSANC6. The PBSA nanocomposites (PBSANCs) with four different C30B loadings of 3, 4, 5, and 6 wt%, were abbreviated as PBSANC3, PBSANC4, PBSANC5, and PBSANC6, respectively. Here we are denoting core by 'c', inner shell by 's1' and outer shell by 's2'.

and the inter-particle distance is much higher than in the other model nanocomposites. Still there are some overlapping of neighboring particles, which increases the stacking of the clay layers. In the case of PBSANC4 (Fig. 8(b)), the dispersion characteristics are almost the same as PBSANC3; however, only the probability of finding neighbors increases. This supports the interpretation drawn from the SAXS analysis.

To have more deeper understanding of the degree of dispersion of silicate layers in PBSA matrix, Image J software was used to analyze STEM images (for each sample ~280 tactoids were considered). For image analysis, the thickness distribution picture was first drawn in power point and then the particle size analysis was carried out by Image J software. Finally, this particle size analysis data was transferred to Kaleida graph to draw a histogram as presented in Fig. 9. In Fig. 9, the number of stacked silicate layers (in %) for the different nanocomposites is plotted against the thickness of the stacked silicate layers (in nm) determined on the basis of the STEM images. It is clear from the figure that for all nanocomposites the minimum thickness of the dispersed silicate layers can be 1.5 nm. This result is relevant with the SAXS analysis. Furthermore, in the case of PBSANC3, the maximum number of the stacked silicate layers possess the thickness in a range of 4.5–

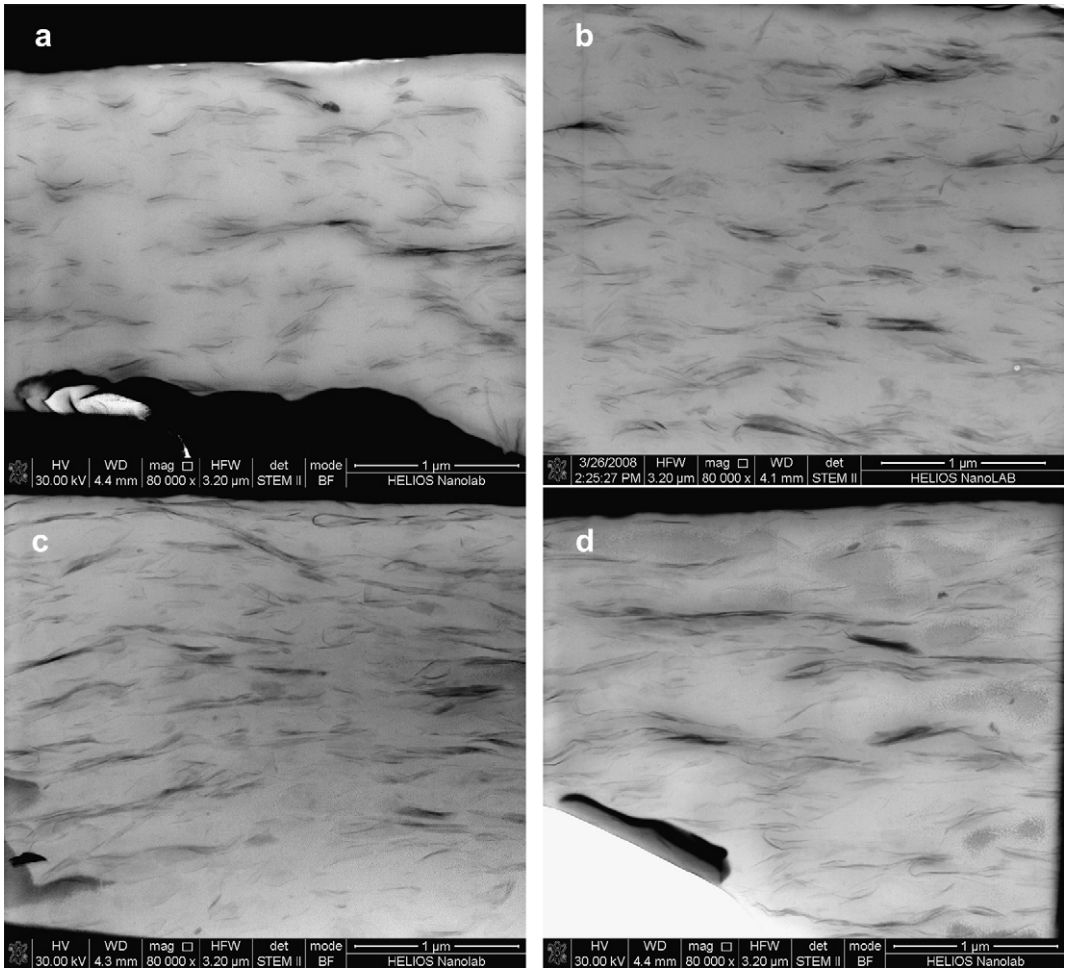

Fig. 8. The bright-field scanning transmission electron microscopy (STEM) images of four different nanocomposite systems, in which black entities represent the dispersed silicate layers: (a) PBSANC3 (containing 3 wt% C30B), (b) PBSANC4 (containing 4 wt% C30B), (c) PBSANC5 (containing 5 wt% C30B), and (d) PBSANC6 (containing 6 wt% C30B).

7.5 nm. In PBSANC4, the percentage of the silicate layers stacking falling in the first two thickness range reduces and the number of stacked silicate layers with higher thickness increases. From the STEM analysis, it is also prominent that for these two nanocomposites (PBSANC3 and PBSANC4) there is a drastic change in intercalated silicate layers' population in neighbouring thickness zone. While, in the case of PBSANC5, the silicate layers population of different thickness range does not change drastically. For PBSANC6, initially the population of silicate layers reduces in the first two thickness zone, but it suddenly increases within 7.5–10.5 and 10.5–13.5 nm. After fitting cubic splines on the histogram it is clear that the nature of the fitting curve changes from Lorentzian to almost Gaussian with increase in C30B loading. The intensity of the peak reduces systematically as the C30B concentration increases up to 5 wt%. Further increase in C30B concentration results higher intense peak. Therefore, it can be concluded that PBSANC5 has splashed cards like flocculated structure. On the other hand, because of the Gaussian fitting of the histogram one can say PBSANC6 possesses nicely dispersed stacked intercalated structure. Again, the peak positions of mainly Lorentzian distributions (i.e., for PBSANC3 to PBSANC5) falls within the thickness range of 4.5–7.5 nm, i.e., on average 6 nm (see Fig. 9). According to SAXS results, the mean number of layers (n) varies between 5.6 and 5.8 with the variation of clay content in the nanocomposites. Therefore, the STEM observations support the conclusions made on the basis of the SAXS analysis.

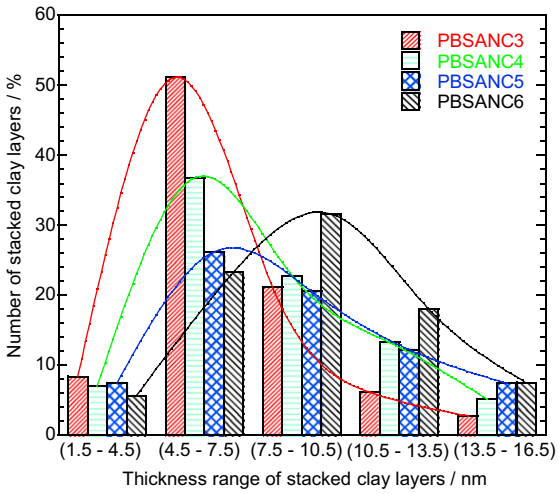

Fig. 9. The number of stacked silicate layers (in %) for the different nanocomposites is plotted against the thickness of the stacked silicate layers (in nm) determined on the basis of the STEM images. Image J software was used to analyze STEM images (for each sample ~280 tactoids were considered). For image analysis, the thickness distribution picture was first drawn in power point and then the particle size analysis was carried out by Image J software. Finally, this particle size analysis data was transferred to Kaleida graph to draw the histogram. The PBSA nanocomposites with four different C30B loadings of 3, 4, 5, and 6 wt%, were abbreviated as PBSANC3, PBSANC4, PBSANC5, and PBSANC6, respectively.

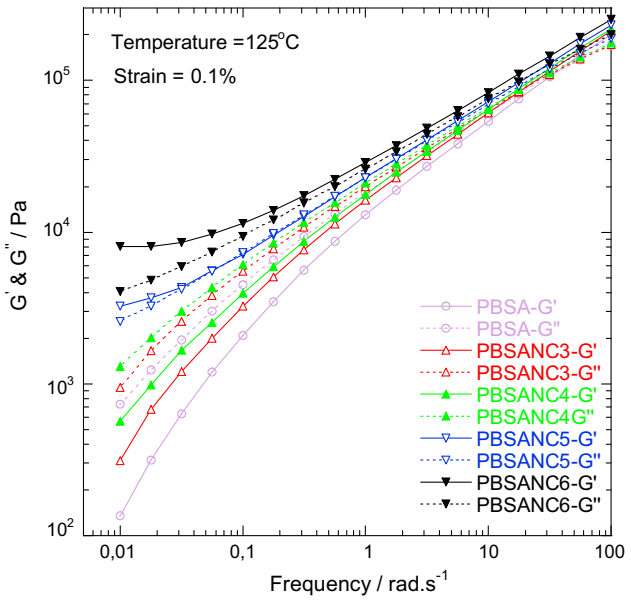

Fig. 10. The angular frequency dependence of storage modulus (G') and loss modulus of pure polymer and various nanocomposite samples. Frequency sweep experiments were conducted at 125 °C with a constant strain value of 0.1%. The PBSA nanocomposites with four different C30B loadings of 3, 4, 5, and 6 wt%, were abbreviated as PBSANC3, PBSANC4, PBSANC5, and PBSANC6, respectively.

4.3. Melt-state rheological properties

Now from the SAXS results and STEM observations, one can say that the concentration of the C30B in the nanocomposites has strong influence on the morphology of the nanocomposites. Therefore, it is expected that the properties of the nanocomposites should change accordingly. The following sub-sections illustrate the material response of the nanocomposites under oscillatory tests in the melt-state.

4.3.1. Frequency sweep tests

The frequency sweeps results are useful to investigate the time-dependent shear behavior since the frequency is the inverse value of the time. The frequency sweep experiments were carried out at 125 °C with a strain amplitude (chosen from the LVE region) of 0.1% in the frequency rage 100–0.01 rad/s. Melt-state rheological properties of various nanocomposites during frequency sweep are summarized in Fig. 10. During frequency sweep measurements in the linear viscoelastic region, the viscous property of nanocomposites shows a dominant nature as long as C30B loading increases up to 4 wt%. In the case of PBSANC5 because of the formation of a flocculated structure (as determined by SAXS and STEM) [48,49], the value of G' is almost equal to G''. However, due to the presence of homogeneously dispersed stacked intercalated silicate layers (refer to the STEM images analyses section), PBSANC6 behaves like a solid material with $G' > G''$. With an increase in C30B loading, clay stacking increases, the flexibility of the samples decreases, and they start to behave like solid materials.

4.3.2. Thixotropic oscillatory tests

To check the material response of the pure PBSA and nanocomposite samples—whether they are showing thixotropic or rheopectic behaviors—oscillatory tests in the three intervals were performed at constant dynamic mechanical conditions. The first interval is known as the reference interval, and here the samples experience oscillation with a very small strain amplitude of 0.1%. The aim is to achieve fairly constant values of G' and G'' for the whole first interval. The second interval is the high shear interval where samples experience oscillation with a very high strain amplitude of 50% in order to break down the internal structure of the samples. In the third region, i.e., in the regeneration interval at very low shear conditions like the first interval, the samples try to recover their initial structures. Fig. 11 shows the time-dependent functions of G' and G'' of PBSA and nanocomposite systems at low shear conditions during structural breakdown and regeneration. From Fig. 11 it is clear that in the first interval, pure PBSA, PBSANC3, and PBSANC4 have a dominant viscous properties since $G' < G''$; however, PBSANC5 and PBSANC6 are showing the opposite trend. In the second interval, the structural breakdown attains higher values with high C30B loading. After breaking the structure in the second interval, the properties of PBSANC5 change. In the third interval, PBSANC5 also shows $G' < G''$ like pure PBSA and the other two nanocomposites such as PBSANC3 and PBSANC4. In the case of PBSANC6, $G' > G''$ in the third interval, however, the difference between the moduli reduces significantly compared to the first interval. The G' values for all studied samples at the end of the three intervals are reported in Table 2. The percent of destruction of structures at the end of the

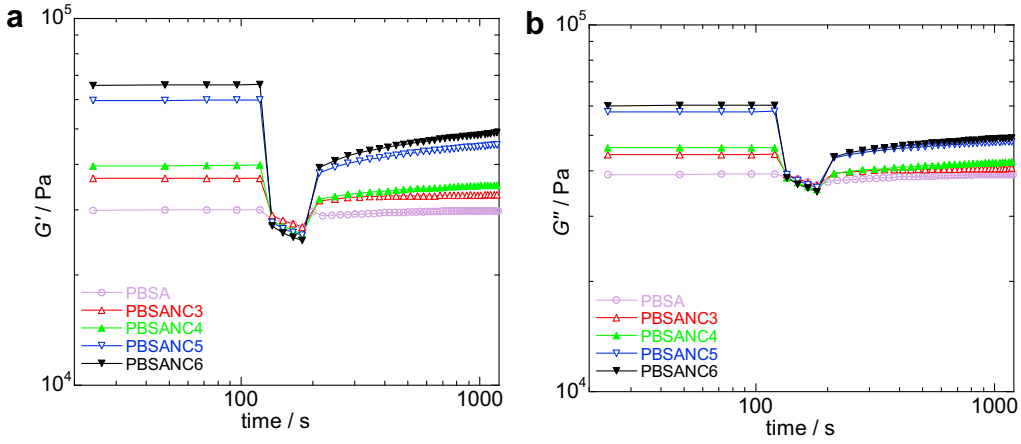

Fig. 11. Time-dependent functions of (a) storage modulus (G') and (b) loss modulus (G'') of pure polymer and nanocomposite samples at low shear condition, during structural breakdown and regeneration. PBSANC3 (containing 3 wt% C30B), PBSANC4 (containing 4 wt% C30B), PBSANC5 (containing 5 wt% C30B), and PBSANC6 (containing 6 wt% C30B).

Table 2
The parameters related to breaking and regeneration of structures during thixotropic oscillation tests.

Sample[a]	G′/Pa (at the end of interval 1)	G′/Pa (at the end of interval 2)	G′/Pa (at the end of interval 3)	Destruction of structure/%	Regeneration of structure/%
PBSA	29915	26969	29915	9.8	9.8
PBSANC3	36534	26573	32694	27.3	16.8
PBSANC4	39929	25797	35207	35.4	23.6
PBSANC5	59998	25607	45284	57.3	32.8
PBSANC6	65572	24860	48764	62.1	36.5

[a] PBSA nanocomposites with four different C30B loadings of 3, 4, 5, and 6 wt%, were correspondingly abbreviated as PBSANC3, PBSANC4, PBSANC5, and PBSANC6, respectively.

second interval and the percent of regeneration of structures at the end of the third interval were estimated according to the equations (20) and (21), respectively and values are also reported in Table 2 [50].

$$\text{destruction} = \frac{G'_{\text{int}-1} - G'_{\text{int}-2}}{G'_{\text{int}-1}} \times 100\% \quad (20)$$

$$\text{regeneration} = \frac{G'_{\text{int}-3} - G'_{\text{int}-2}}{G'_{\text{int}-1}} \times 100\% \quad (21)$$

From the calculated data (see Table 2) it is clear that the pure PBSA chains can fully recover their original structure; however, the ability of PBSA chains to recover the original structure decreases systematically with an increase in C30B loading. This could be due to the change in dispersion characteristic of clay particles in the PBSA matrix with an increase in C30B loading. During the application of a high shear field, it is possible to deform the structures, and pure PBSA chains can achieve the initial entangled state again during the regeneration interval. On the other hand, in the case of nanocomposites, it is easy to break down the original structures by applying a high shear field since in nanocomposites the polymer chains are already in a disentangled state due to the presence of dispersed silicate layers. Furthermore, in nanocomposites when the polymer chains disentangle or cross-linking breaks down due to the high shear field, the orientation of delaminated silicate layers changes simultaneously. During regeneration time, the dispersed clay layers prevent polymer chains from bending and folding. For this reason, it is difficult for nanocomposites to recover original structure within the experimental time. This phenomenon becomes more pronounced for nanocomposites as the clay loading increases.

5. Conclusions

This study proposed an innovative approach for the quantitative analysis of the degree of dispersion of silicate layers in the polymer matrix by SAXS. The SAXS results and STEM observations show that the amount of OMMT loading plays a vital role in controlling the network structure of dispersed silicate layers of nanocomposites and, hence, melt-flow behaviours of nanocomposites. Results also show that the 5 wt% of OMMT is the percolation threshold value to start the formation of the strong flocculated structure of dispersed silicate layers. For this reason, the flow behaviors of nanocomposite containing 5 wt% of OMMT suddenly change with further addition of OMMT.

Acknowledgements

The authors would like to thank the CSIR executive and the DST, South Africa, for financial support. Authors would also like to express their appreciation to Anton Paar SAXS team for scientific comments and Dr D. Wall from FEI company for electron microscopy help.

References

[1] Pavlidou S, Papaspyrides CD. Prog Polym Sci 2008;33:1119.
[2] Paul DR, Robeson LM. Polymer 2008;49:3187.
[3] Sinha Ray S, Bousmina M. Prog Mater Sci 2005;50:962.
[4] Sinha Ray S, Okamoto M. Prog Polym Sci 2003;28:1539.
[5] Fischer H. Mater Sci Eng 2003;C23:763.
[6] Alexandre M, Dubois P. Mater Sci Eng 2000;R28:1.
[7] Bafna A, Beaucage G, Mirabella F, Mehta S. Polymer 2003;44:1103.
[8] Loo LS, Gleason KK. Macromolecules 2003;36:2587.
[9] VanderHart DL, Asano A, Gilman JW. Macromolecules 2001;34:3819.
[10] Saito T, Okamoto M, Hiroi R, Yamamoto M, Shiroi T. Polymer 2007;48:4143.
[11] Davis RD, Bur AJ, McBrearty M, Lee YH, Gilman JW, Start PR. Polymer 2004;45:6487.
[12] Morgan AB, Gilman JW. J Appl Polym Sci 2003;87:1329.
[13] Krishnamoorti R, Yurekli K. Curr Opin Colloid Interface Sci 2001;6:464.
[14] Thiyagarajan P. J Appl Crystallogr 2003;36:373.
[15] Ho DL, Briber RM, Glinka C. J Chem Mater 1923;2001:13.
[16] Schaefer DW, Pekala R, Beaucage G. J Non-Cryst Solids 1995;186:159.
[17] Hua DW, Anderson J, Di Gregorio J, Smith DM, Beaucage G. J Non-Cryst Solids 1995;186:142.
[18] (a) Xu Y, Brittain WJ, Vaia RA, Price G. Polymer 2006;47:4564;
(b) Koerner H, Misra D, Tan A, Drummy L, Mirau P, Vaia RA. Polymer 2006;47:3426;
(c) Lin-Gibson S, Kim H, Schmidt G, Han CC, Hobbie EK. J Colloid Interface Sci 2004;274:515;
(d) Dillon DR, Tenneti KK, Li CY, Ko FK, Sics I, Hsiao BS. Polymer 2006;47:1678;
(e) Vaia RA, Price G, Ruth PN, Nguyen HT, Lichtenhan J. Appl Clay Sci 1999;15:67;
(f) Bae WJ, Kim KH, Jo WH, Park YH. Polymer 2005;46:10085;
(g) Jeong EH, Yang J, Hong JH, Kim TG, Kim JH, Youk JH. Eur Polym J 2007;43:2286.
[19] Koerner H, Liu W, Alexander M, Mirau P, Dowty H, Vaia RA. Polymer 2005;46:4405.
[20] Lincoln DM, Vaia RA, Wang Z-G, Hsiao BS, Krishnamoorti R. Polymer 2001;42:9975.
[21] Ganguli S, Dean D, Jordan K, Price G, Vaia RA. Polymer 2003;44:1315.
[22] Chin IJ, Thurn-Albrecht T, Kim H-C, Russell TP, Wang J. Polymer 2001;42:5947.
[23] Nawani P, Desai P, Lundwall M, Gelfer MY, Hsiao BS, Rafailovich M, et al. Polymer 2007;48:827.
[24] Fu BX, Gelfer MY, Hsiao BS, Phillips S, Viers B, Blanski R, et al. Polymer 2003;44:1499.
[25] Medellin-Rodriguez FJ, Burger C, Hsiao BS, Chu B, Vaia RA, Phillips S. Polymer 2001;42:9015.
[26] (a) Marigo A, Causin V, Marega C, Ferrari P. Polym Int 2001;2004:53;
(b) Causin V, Marega C, Marigo A, Ferrara G, Idiyatullina G, Fantinel F. Polymer 2006;47:4773;
(c) Causin V, Marega C, Marigo A, Ferrara G. Polymer 2005;46:9533.
[27] Hosemann R, Bagchi SN. Direct analysis of diffraction by matter. Amsterdam: North Holland; 1962.
[28] Preschilla N, Sivalingam G, Abdul Rasheed AS, Tyagi S, Biswas A, Bellare JR. Polymer 2008;49:4285.
[29] Yoonessi M, Toghiani H, Daulton TL, Lin J-S, Pittman Jr CU. Macromolecules 2005;38:818.
[30] Drummy LF, Wang YC, Schoenmakers R, May K, Jackson M, Koerner H, et al. Macromolecules; 2008:41–2135.
[31] Ishioka D. Biopolymers, polyesters III. Applications and commercial products, vol. 4. Weinheim: Wiley-VCH Verlag Gmbh; 2002. p. 275;
Nikolic MS, Djonlagic J. Polym Degrad Stab 2001;74:263.
[32] Fujimaki T. Polym Degrad Stab 1998;59:209.
[33] Very roughly calculated using group contribution method of Fredor Krevelen DWV. Properties of polymer. Amsterdam, The Netherlands: Elsevier; 1990.
[34] Mittelbach R, Glatter O. J Appl Crystallogr 1998;31:600.

[35] Schnablegger H, Singh Yashveer. A practical guide to small angle X-ray scattering. Austria: Anton Par GmbH; 2006.
[36] Glatter O, Kratky O. Small angle X-ray scattering. London: 1982.
[37] Glatter O. Acta Phys Austriaca 1977;47:83.
[38] Glatter O. J Appl Crystallogr 1977;10:415.
[39] Bergmann A, Fritz G, Glatter O. J Appl Crystallogr 2000;33:1212.
[40] Brunner-Popela J, Glatter O. J Appl Crystallogr 1997;30:431.
[41] Weyerich B, Brunner-Popela J, Glatter O. J Appl Crystallogr 1999;32:197.
[42] Guinier A. X-ray diffraction in crystals, imperfect crystals and amorphous bodies. Ontario, Canada: General Publishing Company; 1994.
[43] Caillé A, Seances CR. Acad Sci Ser 1972;B274:891;
Also see the erratum in Gennes PG. The physics of liquid crystals. London: Oxford University Press; 1974. p. 336, Ref. [20].
[44] (a) Zhang R, Tristram-Nagle S, Sun W, Headrick RL, Irving TC, Suter RM, et al. Biophys J 1996;70:349;
(b) Zhang R, Suter RM, Nagle JF. Phys Rev E 1994;50:5047.
[45] Frühwirth T, Fritz G, Freiberger N, Glatter O. J Appl Crystallogr 2004;37:703.
[46] (a) Glatter O. J Appl Crystallogr 1981;14:101;
(b) Glatter O. J Appl Crystallogr 1988;21:886;
(c) Glatter O, Hainisch B. J Appl Crystallogr 1984;17:435.
[47] Schnablegger H, Rien DH, Rempp P, Cohen RE. J Polym Eng 1996;6:1.
[48] Sinha Ray S, Maiti P, Okamoto M, Yamada K, Ueda K. Macromolecules 2002;35:3104.
[49] Sinha Ray S, Okamoto K, Okamoto M. Macromolecules 2003;36:2355.
[50] Mezger TG. The rheology handbook. 2nd ed. Germany: Vincentz; 2006.